

## Pore fluid effects on S-wave attenuation caused by wave-induced fluid flow

Beatriz Quintal<sup>1</sup>, Holger Steeb<sup>2</sup>, Marcel Frehner<sup>1</sup>, Stefan M. Schmalholz<sup>3</sup>, and Erik H. Saenger<sup>1</sup>

### ABSTRACT

We studied seismic attenuation of P- and S-waves caused by the physical mechanism of wave-induced fluid flow at the mesoscopic scale. Stress relaxation experiments were numerically simulated by solving Biot's equations for consolidation of 2D poroelastic media with finite-element modeling. The experiments yielded time-dependent stress-strain relations that were used to calculate the complex moduli from which frequency-dependent attenuation was determined. Our model consisted of periodically distributed circular or elliptical heterogeneities with much lower porosity and permeability than the background media, which contained 80% of the total pore space of the media. This model can represent a hydrocarbon reservoir, where the porous background is fully saturated with oil or gas and the low-porosity regions are always saturated with water. Three different saturation scenarios were considered: oil-saturated (80% oil, 20% water), gas-saturated (80% gas, 20% water), and fully water-saturated media.

Varying the dry bulk and shear moduli in the background and in the heterogeneities, a consistent tendency was observed in the relative behavior of the S-wave attenuation among the different saturation scenarios. First, in the gas-saturated media the S-wave attenuation was very low and much lower than in the oil-saturated or in the fully water-saturated media. Second, at low frequencies the S-wave attenuation was significantly higher in the oil-saturated media than in the fully water-saturated media. The P-wave attenuation exhibited a more variable relative behavior among the different saturation degrees. Based on the mechanism of wave-induced fluid flow and on our numerical results, we suggest that S-wave attenuation could be used as an indicator of fluid content in a reservoir. Additionally, we observed that impermeable barriers in the background can cause a significant increase in S-wave attenuation. This suggests that S-wave attenuation could also be an indicator of permeability changes in a reservoir due to, for example, fracturing operations.

### INTRODUCTION

Attenuation of seismic waves in partially saturated porous rocks is of great interest because it recently has been observed that oil and gas reservoirs frequently exhibit high P-wave attenuation, especially at low seismic frequencies (Rapoport et al., 2004; Chapman et al., 2006; Quintal et al., 2011a). When well understood, attenuation effects can help in the interpretation and inversion of seismic data, especially for inferring pore-fluid type and saturation in a reservoir. A good understanding of fluid effects on attenuation can be achieved by systematic numerical (e.g., Rubino et al., 2011) and laboratory (e.g., Paffenholz and Burkhardt, 1989; Behura et al., 2009) studies. In this paper, we present a numerical study of

attenuation caused by the physical mechanism known as wave-induced fluid flow (e.g., Pride et al., 2004).

At low seismic frequencies (1–100 Hz), wave-induced fluid flow caused by fluid-pressure differences between mesoscopic-scale heterogeneities is a major cause of P-wave attenuation in a partially saturated porous rock (White, 1975; Pride et al., 2004; Müller et al., 2010). The mesoscopic scale is the scale much larger than the pore size but much smaller than the wavelength. A partially saturated rock is approximated by a poroelastic medium with regions fully saturated by one fluid and other regions fully saturated by another fluid. This is frequently referred to as patchy saturation. Mesoscopic-scale heterogeneities can also occur in the porosity

Manuscript received by the Editor 29 June 2011; revised manuscript received 6 January 2012; published online 5 April 2012.

<sup>1</sup>ETH Zurich, Department of Earth Sciences, Zurich, Switzerland. E-mail: beatriz.quintal@erdw.ethz.ch; marcel.frehner@erdw.ethz.ch; erik.saenger@erdw.ethz.ch.

<sup>2</sup>Ruhr-University Bochum, Mechanics-Continuum Mechanics, Bochum, Germany. E-mail: holger.steeb@rub.de.

<sup>3</sup>University of Lausanne, Institute of Geology and Palaeontology, Lausanne, Switzerland. E-mail: stefan.schmalholz@unil.ch.

© 2012 Society of Exploration Geophysicists. All rights reserved.

and/or other solid frame properties, and they are taken into account by (and generally referred to as) double-porosity models (Pride and Berryman, 2003a, 2003b; Pride et al., 2004). Patchy saturation and double porosity are two models for attenuation due to wave-induced fluid flow at the mesoscopic scale.

Many analytical solutions have been derived to quantify P-wave attenuation in media with patchy saturation or double porosity for idealized geometries and distributions of the heterogeneities (White, 1975; White et al., 1975; Norris, 1993; Johnson, 2001; Pride and Berryman, 2003a, 2003b; Müller and Gurevich, 2004; Pride et al., 2004; Vogelaar et al., 2010). Concerning S-wave attenuation, the only analytical solution available has recently been derived by Liu et al. (2009) for the attenuation of S-waves due to scattering by mesoscopic-scale spherical inclusions embedded in an infinite poroelastic media. In this solution, the results for S-wave attenuation are superimposed by sharp peaks that represent resonances. Numerical modeling is therefore an important tool to calculate S-wave attenuation, in addition to P-wave attenuation, in media with heterogeneities of complicated, realistic geometries (e.g., obtained from tomographic images of rock samples).

Masson and Pride (2007) propose a methodology to numerically calculate P- and S-wave attenuation due to wave-induced fluid flow in a unit cell (representative elementary volume [REV]) containing mesoscopic-scale heterogeneities. They suggest a quasi-static creep test to solve Biot's equations for wave propagation (Biot, 1962) in poroelastic media using the finite-difference method. Recently, Rubino et al. (2009), Wenzlau et al. (2010), and Quintal et al. (2011b) have also presented quasi-static numerical strategies to calculate seismic attenuation due to wave-induced fluid flow. Rubino et al. (2009) compute oscillatory compressibility tests in the frequency domain and solve Biot's dynamic equations for wave propagation using the finite-element method. Wenzlau et al. (2010) compute relaxation tests to solve Biot's equations for wave propagation using Abaqus software (Dassault Systèmes), which incorporates the finite-element method. Quintal et al. (2011b) compute creep tests using the finite-element method to solve Biot's equations for consolidation (Biot, 1941) of poroelastic media in

the displacement-pressure ( $u$ - $p$ ) formulation. No inertia terms appear in the equations for consolidation, the computed attenuation is solely due to flow of the viscous fluid, which is controlled by the gradient of the pore-fluid pressure. Excluding the inertial forces at low seismic frequencies is a valid approximation because they are negligible for typical properties of rocks and saturating fluids at these frequencies (e.g., Bourbié et al., 1987). In this paper, we use the algorithm described by Quintal et al. (2011b) to compute the frequency-dependent seismic P- and S-wave attenuation caused by wave-induced fluid flow at the mesoscopic scale.

Pore-fluid effects have been studied for P-wave attenuation in patchy-saturated models where the rock frame is homogeneous and heterogeneities occur in fluid saturation. For such models, P-wave attenuation can be significant when one of the two fluids is much more compressible than the other and the more compressible fluid saturates the medium in small amounts, such as around 10% (Quintal et al., 2009). In such patchy-saturated models with a homogeneous rock frame, S-waves are not attenuated (e.g., Pride et al., 2004). Attenuation of S-waves occurs as a consequence of heterogeneities in the solid frame but is also function of fluid properties (Berryman and Wang, 2001). According to Berryman and Wang (2001), external shear boundary conditions can lead to local compression in some regions containing liquid; because the liquid can support compression (but not shear), it stores some of the energy resulting from the shear boundary conditions. Therefore, the pore fluid has an influence on the attenuation of S-waves. Although some authors have calculated S-wave attenuation due to wave-induced fluid flow in media of heterogeneous solid frame (e.g., Masson and Pride, 2007; Liu et al., 2009; Rubino et al., 2009; Wenzlau et al., 2010), a systematic study on the effects of the pore fluid on S-wave attenuation has not been presented so far. This is necessary for a better understanding of S-wave behavior in fluid-saturated rocks and its possible applications.

In this article, we combine fluid-saturation heterogeneities (patchy saturation) with rock-frame heterogeneities (double porosity). The main objective is to study the effect of the pore fluid on P- and S-wave attenuation. Our model consists of periodically distributed circular or elliptical heterogeneities with much lower porosity and permeability than the continuous background medium, which contains 80% of the total pore space of the medium. The heterogeneities are always fully saturated with water, whereas the background medium is fully saturated with gas, oil, or water. Our model can be representative of a hydrocarbon reservoir where water preferentially saturates regions of small pores but the hydrocarbon (gas or oil) saturates areas of reasonably high porosity. We compare attenuation in two media with high degrees of hydrocarbon saturation (80% oil or gas, 20% water) with a medium fully saturated with water, paying special attention to the S-wave attenuation.

## METHODOLOGY

We use the finite-element method to solve Biot's equations for consolidation (Biot, 1941) in the  $u$ - $p$  formulation (Zienkiewicz and Shiomi, 1984). Using the  $u$ - $p$  formulation allowed us to implement the boundary condition for zero fluid flow (undrained test) in the weak formulation of Biot's equations. Therefore, all of our simulations are performed over a numerical model with undrained boundaries. The algorithm uses an unstructured mesh (e.g., Figure 1) with Delaunay triangulation (Shewchuk, 2002). Each triangular element with quadratic shape functions consists of seven nodal points on

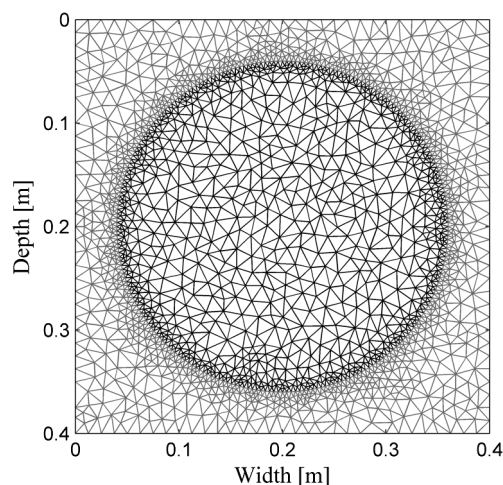


Figure 1. Unstructured finite-element mesh of the unit cell. Black and grey elements inside and outside the circular heterogeneity have different petrophysical properties (Tables 2 and 3). The spatial resolution of the mesh is higher close to the interface between the heterogeneity and the background.

which the solid displacements and fluid pressure are calculated. The spatial resolution of the mesh can strongly vary. Such an unstructured mesh makes the algorithm accurate for simulations in media with heterogeneities of arbitrary geometries. Additionally, time increments of variable length make the algorithm computationally efficient for the applied boundary conditions. In our simulations, the length of the time increments is constant during the first 0.1% of the total simulated time, and afterward it increases linearly with time. Very small time steps at the beginning are necessary to accurately resolve the complex moduli at high frequencies; the total time should be large enough to ensure accuracy at low frequencies. The algorithm is described in detail by Quintal et al. (2011b). They perform benchmark tests showing that the algorithm is accurate and stable, and that it is well suited to determine the complex moduli over a very broad frequency range (i.e., at least six orders of magnitude).

Here, we applied this quasi-static finite-element algorithm to relaxation tests on 2D poroelastic samples with mesoscopic-scale heterogeneities. These tests yield the time-dependent stress and strain, averaged for each time step over the area of the numerical model. In a postprocessing step, we calculate the time derivatives of the stress and strain, and convert them to the frequency domain using a Fourier transform. The frequency-dependent stress and strain rates are used to calculate the complex P-wave modulus  $H$ , and the complex shear modulus  $\mu$ . This will be described in more detail in the next section. From the complex moduli  $H$  and  $\mu$ , we calculate the P- and S-wave quality factors

$$Q_P = \frac{\text{Re}(H)}{\text{Im}(H)} \quad (1)$$

and

$$Q_S = \frac{\text{Re}(\mu)}{\text{Im}(\mu)}, \quad (2)$$

respectively, where Re and Im denote the real and imaginary parts. The inverse of the quality factor  $1/Q$  is a measure of attenuation (e.g., Carcione, 2007).

P- and S-wave attenuation in our experiments is caused by fluid flow induced by pressure differences between regions of different compliances, which are due to different fluid and/or solid frame properties. Here, we calculate attenuation and dispersion in poroelastic medium with periodically distributed mesoscopic-scale heterogeneities. For example, the REV of a medium containing periodically distributed circular heterogeneities is the unit cell shown in Figure 1. The numerical model in our experiments consists of a single unit cell or a periodic distribution of unit cells.

## MEDIA WITH CIRCULAR HETEROGENEITIES

### Experimental setup

To calculate P- and S-wave attenuation for a medium containing periodically distributed circular heterogeneities whose unit cell is shown in Figure 1, we used two experimental setups for the relaxation experiments: uniaxial compression with constricting walls parallel to the compression direction (Figure 2a) and simple shear (Figure 2b). In each experiment, a time-dependent function  $S(t)$  (Figure 3) is attributed at the boundary of the model to the

displacement, with direction and amplitude indicated by the arrows in Figure 2.

In the uniaxial compression test (Figure 2a), the function  $S(t)$  is attributed to the displacement in the  $z$ -direction at the top boundary of the numerical model and zero is attributed to the displacement in the  $z$ -direction at the bottom and to the displacement in the  $x$ -direction at the left and right boundaries. We obtain from this experiment the time-dependent normal strain and the total normal stress in the  $z$ -direction, averaged over the area of the numerical model in each time step. A partial time derivative is applied to these results and, subsequently, the time-dependent normal strain and stress rates in the  $z$ -direction are converted into the frequency domain, yielding  $\hat{\epsilon}_{zz}$  and  $\hat{\sigma}_{zz}$ , respectively, used to calculate the complex and frequency-dependent component of the stiffness matrix:

$$C_{33} = \frac{\hat{\sigma}_{zz}}{\hat{\epsilon}_{zz}}. \quad (3)$$

The component  $C_{33}$  is equal to the P-wave modulus  $H$  at  $0^\circ$  incidence (angle between the wave vector and the vertical axis, or  $z$ -axis).

In the simple shear test (Figure 2b), the function  $S(t)$  is attributed to the displacement in the  $x$ -direction at the top and bottom boundaries of the numerical model, with opposite signs, it is attributed with a linear  $z$ -dependent amplitude (varying from the value at

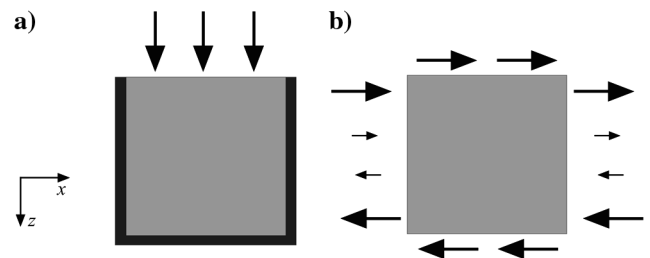


Figure 2. Sketch of the relaxation experiments: (a) uniaxial compression in the  $z$ -direction and (b) simple shear. The arrows indicate direction and magnitude of the displacements applied at the boundaries.

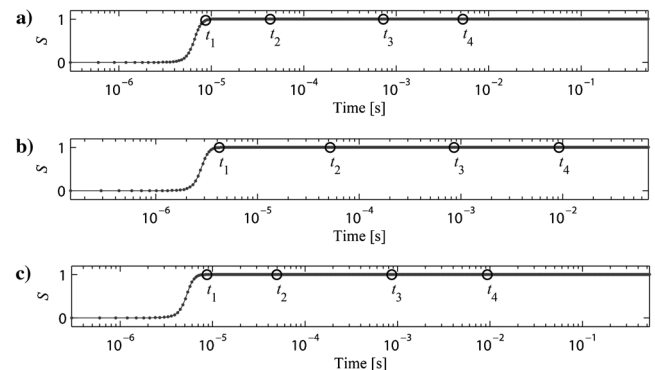


Figure 3. Evolution of the boundary conditions  $S(t)$ , normalized by their maximum values, for the three experiments illustrated in Figure 4. The functions  $S(t)$  are shown with time in logarithmic scale. The times  $t_1$ ,  $t_2$ ,  $t_3$ , and  $t_4$  at which the snapshots in Figure 4 were taken are indicated in the curves shown in (a-c), which, respectively, refer to Figure 4a, 4b, and 4c.

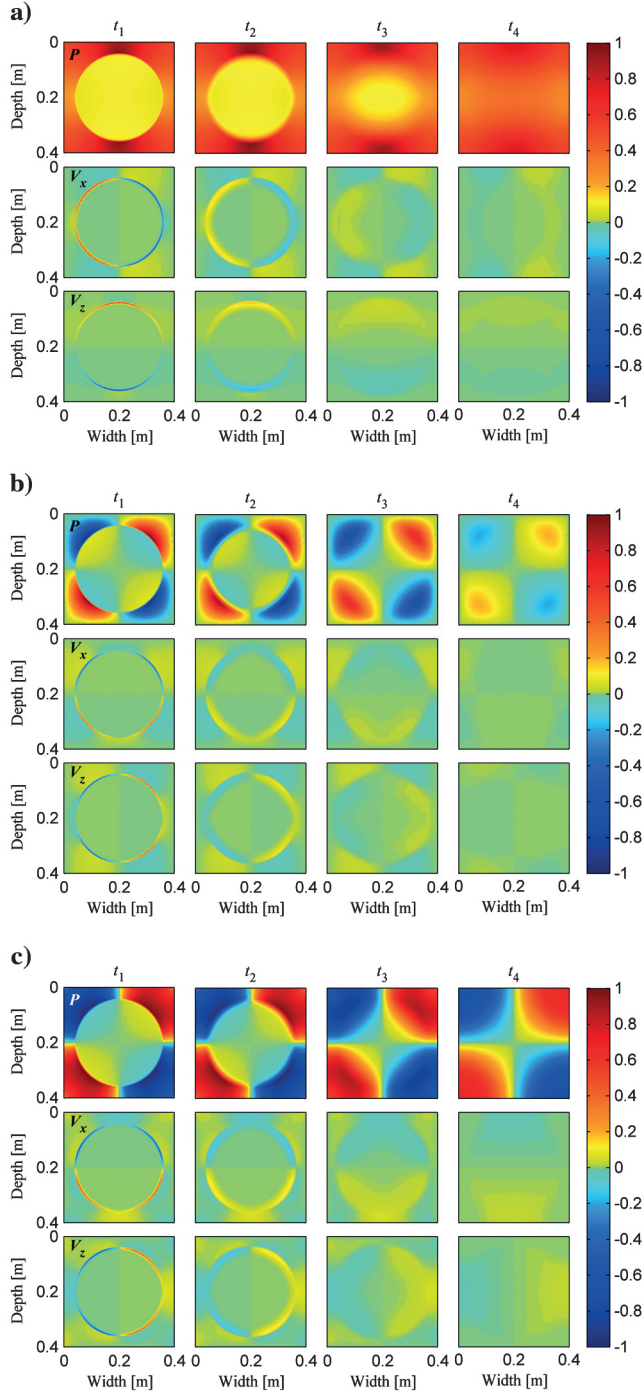


Figure 4. Snapshots at times  $t_1$ ,  $t_2$ ,  $t_3$ , and  $t_4$  of the pore-fluid pressure field  $P$ , the fluid velocity in the  $x$ -direction  $V_x$ , and the fluid velocity in the  $z$ -direction  $V_z$ , normalized by their maximum values, for three relaxation experiments: (a) a compression test with the numerical model consisting of a single unit cell (i.e., one REV, Figure 1), (b) a simple-shear test with the numerical model consisting of 25 unit cells spatially arranged in a  $5 \times 5$  array, and (c) a simple-shear test with the numerical model consisting of a single unit cell. The evolution of the boundary conditions is shown in Figure 3. The frame properties are described by case A (Table 3). The saturation scenario corresponds to oil saturation in the background (Table 2). The results of the simulations illustrated in (a-c), are shown in Figure 5a, 5b, and 5c, respectively (for case A and oil saturation).

the top to the value at the bottom) to the displacement in the  $x$ -direction at the right and left boundaries, and the displacement in the  $z$ -direction is fixed to zero at all the four boundaries. Time-dependent shear strain and stress in the  $x$ -direction is obtained from this experiment. A partial time derivative is applied to these results and, subsequently, the time-dependent shear strain and stress rates in the  $x$ - $z$ -directions are converted into the frequency domain, yielding  $\hat{\epsilon}_{xz}$  and  $\hat{\sigma}_{xz}$ , respectively. We calculate the complex and frequency-dependent component of the stiffness matrix with

$$C_{44} = \frac{1}{2} \frac{\hat{\sigma}_{xz}}{\hat{\epsilon}_{xz}}, \quad (4)$$

where  $C_{44}$  is equal to the shear modulus  $\mu$  at  $0^\circ$  incidence.

The complex and frequency-dependent moduli  $H$  and  $\mu$  (equations 3 and 4) are used to calculate the P- and S-wave quality factors (equations 1 and 2), respectively. Our main purpose is to quantify fluid effects on P- and S-wave attenuation in media containing periodically distributed mesoscopic-scale heterogeneities in the solid frame (Table 3). In our model, the heterogeneities are circular and characterized by low permeability and low porosity. They are embedded in a continuous background medium of high permeability and high porosity. The heterogeneities are always fully saturated with water, and the background is saturated with oil, gas, or water (Table 2). This model can represent a hydrocarbon reservoir where water (the wetting fluid) is not displaced from regions of small pores due to capillary effects. The unit cell of this model is a 40-cm side square, and the radius of the circular heterogeneity is 16 cm (Figure 1). The circle occupies 50% of the unit cell. Because of the different porosities in the heterogeneity and in the background, the pore space in the background corresponds to 80% of the total pore space in the medium. We perform simulations considering the background fully saturated with oil, gas, or water, corresponding to three saturation scenarios: oil-saturated medium (80% oil, 20% water), gas-saturated medium (80% gas, 20% water), and fully water-saturated medium. Four sets of parameters are considered for the solid frame of the rock, differing only by the bulk modulus of the dry frame  $K_d$  and the shear modulus of the dry frame  $\mu_d$  (cases A–D in Table 3).

The petrophysical parameters describing the solid frame (cases A–D, Table 3) were arbitrarily combined to represent strong variations in the rock that could be related, for example, to the degree of

Table 1. Symbols used for the petrophysical parameters.

Symbol	Definition
$\rho_s$	Density of the grains
$K_s$	Bulk modulus of the grains
$\Phi$	Porosity
$k$	Permeability
$K_d$	Bulk modulus of the dry frame
$\mu_d$	Shear modulus of the dry frame
$\rho_f$	Density of the fluid
$\eta$	Viscosity of the fluid
$K_f$	Bulk modulus of the fluid

cementation and/or mineralogical composition. In case A, the solid frame in the heterogeneity is much stiffer (larger  $K_d$  and  $\mu_d$ ) than in the background. In cases B and C, the solid frame in the heterogeneity is stiffer (larger  $K_d$  and  $\mu_d$ ) than in the continuous background, as in case A, but the contrasts in frame compressibility between the heterogeneity and the background are lower than in case A. Case B introduces a stiffer model (larger values of  $K_d$  and  $\mu_d$  in the two regions), while case C introduces a more compliant model (lower values of  $K_d$  and  $\mu_d$  in the two regions). In case D, opposite to cases A–C, the solid frame in the heterogeneity is more compliant (lower  $K_d$  and  $\mu_d$ ) than in the continuous background.

For cases A–D and the three saturation scenarios, we perform three sets of relaxation experiments: one set of uniaxial compression tests (Figure 2a), where the numerical model is a single unit cell, and two sets of simple-shear relaxation tests (Figure 2b), where the two numerical models consist of (1) 25 unit cells spatially arranged in a  $5 \times 5$  array and (2) a single unit cell.

### Simulations and results

Figure 4 shows snapshots of three relaxation experiments with the oil-saturated medium and case A, for the pore-fluid pressure field  $P$ , the fluid velocity in the  $x$ -direction  $V_x$ , and the fluid velocity in the  $z$ -direction  $V_z$ . The snapshots in Figure 4a correspond to a compression test with a numerical model consisting of a single unit cell (Figure 1). The normal strain and the total normal stress in the  $z$ -direction obtained from this experiment are averaged over the area of the unit cell. The snapshots in Figure 4b correspond to a simple shear test with a numerical model composed of a  $5 \times 5$  array of unit cells. The shear strain and stress in the  $x$ - $z$ -directions calculated from this experiment are averaged over the area of only the single cell located in the middle of the array. This is done to avoid the effect of the undrained boundaries and to simulate a medium with periodically distributed circular heterogeneities embedded in a homogeneous background. The snapshots in Figure 4c correspond to a simple shear test with a numerical model consisting of only one cell (Figure 1). The shear strain and stress in the  $x$ - $z$ -directions are averaged over the area of the unit cell. Figure 4a, 4b, and 4c shows the pore-fluid pressure differences (snapshots for  $P$ ) induced by compression and simple-shear as well as the corresponding fluid flow (snapshots for  $V_x$  and  $V_z$ ). The time-dependent functions used for the simulations illustrated in Figure 4a, 4b, and 4c are shown in Figure 3a, 3b, and 3c, respectively. The snapshots correspond to the times  $t_1$ ,  $t_2$ ,  $t_3$ , and  $t_4$  indicated in Figure 3. The results from the simulations illustrated in Figure 4a, 4b, and 4c respectively, are, shown in Figure 5a, 5b, and 5c (only the curves for case A and oil saturation) for the real part of the P-wave modulus  $H$ , and the P-wave quality factor  $Q_p$  (Figure 5a) and for the real part of the shear modulus  $\mu$ , and the S-wave quality factor  $Q_s$  (Figure 5b and 5c).

The results from the uniaxial compression tests with a single unit cell for cases A–D and the three saturation scenarios are shown in Figure 5a for the real part of the P-wave modulus  $H$  and the P-wave quality factor  $Q_p$ . These results are equivalent to results from compression tests with a numerical model consisting of an array of several unit cells (not shown here). This is because in the compression experiments, the pressure gradient is negligible at the boundaries separating the unit cells in a periodic medium (e.g., Figure 4a) and, consequently, the fluid flow across the boundaries is also negligible. Therefore, in this case, a single unit cell with undrained

boundaries is sufficient to approximate a medium with periodically distributed circular heterogeneities embedded in a homogeneous background.

The results from the simple shear tests, for cases A–D and the three saturation scenarios with a numerical model consisting of a  $5 \times 5$  array of unit cells and from the simple shear tests for a single unit cell are shown in Figure 5b and 5c, respectively, for the real part of the shear modulus  $\mu$  and the S-wave quality factor  $Q_s$ . In the simple shear experiments, there is a significant pressure gradient across the boundaries between unit cells in a periodic medium (e.g., Figure 4b and 4c); therefore, the fluid flow across the boundaries is significant. This causes the results of the simple shear test using a periodic model ( $5 \times 5$  array of unit cells, Figure 5b) to be considerably different than the results of such a test using a single unit cell (Figure 5c). The S-wave attenuation is significantly higher when the numerical model consists of a single unit cell. Effectively, the difference between the two models causing such an increase in S-wave attenuation is the undrained boundary condition (e.g., Figure 4b and 4c). The numerical model consisting of a single unit cell can represent a medium with periodically distributed circular heterogeneities having impermeable barriers between the unit cells.

**Table 2. Physical properties of the fluids (Batzle and Wang, 1992). Symbols are defined in Table 1.**

Fluid	Water	Oil	Gas
$\rho_f$ (kg/m <sup>3</sup> )	1010	880	160
$\eta$ (Pa-s)	0.001	0.02	$2 \times 10^{-5}$
$K_f$ (GPa)	2.4	1.4	0.04

**Table 3. Physical properties of the solid frame. Symbols are defined in Table 1.**

Region	Heterogeneity	Background
$\rho_s$ (kg/m <sup>3</sup> )	2700	2700
$K_s$ (GPa)	40	48
$\Phi$ (%)	6	26
$k$ (mD)	40	1000
Case A		
$K_d$ (GPa)	36	4
$\mu_d$ (GPa)	32	2
Case B		
$K_d$ (GPa)	36	10
$\mu_d$ (GPa)	32	8
Case C		
$K_d$ (GPa)	10	4
$\mu_d$ (GPa)	8	2
Case D		
$K_d$ (GPa)	4	10
$\mu_d$ (GPa)	2	8

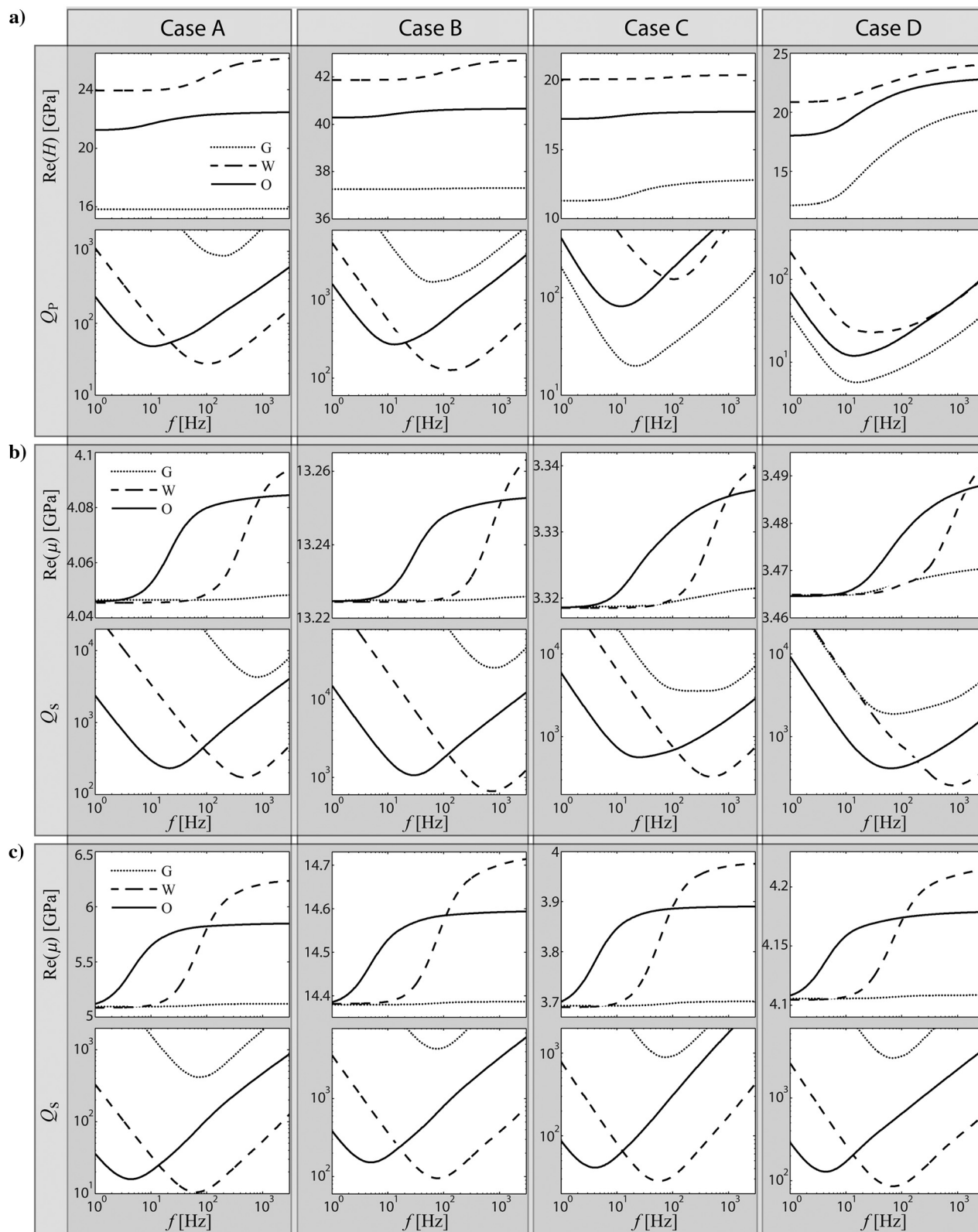


Figure 5. Numerical results for (a) the real part of the P-wave modulus  $H$  and the P-wave quality factor  $Q_p$  obtained from a compression test for a numerical model consisting of a single unit cell (Figure 1); (b) and (c) the real part of the shear modulus  $\mu$  and the S-wave quality factor  $Q_s$  obtained from (b) a simple-shear test for a numerical model consisting of a  $5 \times 5$  array of unit cells and from (c) a simple-shear test for a numerical model consisting of a single unit cell. The petrophysical parameters for the solid frame are given in Table 3 for cases A–D, and the fluid properties are given in Table 2. The legend terms refer to the three saturation scenarios: 80% gas, 20% water (G); 100% water (W); and 80% oil, 20% water (O).

The numerical model consisting of a  $5 \times 5$  array of unit cells (Figure 5b) represents a periodic medium having no such barriers in the background. In this case, the effect of the undrained boundary condition is avoided by using stress and strain fields only from the single unit cell in the center of the model to calculate S-wave attenuation. The impermeable barriers cause an increase of about one order of magnitude in the S-wave attenuation and a shift of about one order of magnitude of the  $Q_S$  curves to lower frequencies.

In Figure 5b and 5c, we also observe that the real part of the shear modulus  $\mu$  at the low-frequency (quasi-static) limit is independent of the properties of the saturating fluid. However, for higher frequencies, the value of  $\text{Re}(\mu)$  changes with changing fluid saturation. This difference (i.e., dispersion) is a consequence of S-wave attenuation, according to the Kramers-Kronig relations (Mavko et al., 2009). Moreover, despite the differences in the rock-frame properties in cases A–D or the presence of impermeable barriers, we observe approximately the same relative behavior of the S-wave attenuation among the three different saturation scenarios in Figure 5b and 5c. In other words, all eight plots for  $Q_S$  exhibit a similar relative position of the three curves. One feature of this relative behavior is that the S-wave attenuation in the gas-saturated media is very low and much lower than in the oil-saturated or in the fully water-saturated media. Second, at low frequencies, the S-wave attenuation is significantly higher in the oil-saturated media than in the fully water-saturated media, although the maximum value of S-wave attenuation is higher in the fully water-saturated media. More precisely, at frequencies equal to or lower than the transition frequencies of  $Q_S$  in the oil-saturated media, the S-wave attenuation is about one order of magnitude higher in the oil-saturated media than in the fully water-saturated media, and the transition frequencies of  $Q_S$  in the oil-saturated media are about 15 times lower than the transition frequencies of  $Q_S$  in the fully water-saturated media. The transition frequency is the frequency at which the minimum value of the quality factor occurs.

For the P-wave attenuation (Figure 5a), on the other hand, a more variable relative behavior among the three different saturation scenarios is observed in cases A–D. For example, in two of the four models, cases A and B, the P-wave attenuation in the gas-saturated media is lower than in the fully water-saturated and in the oil-saturated media, whereas in the other two models, cases C and D, it is higher than in the fully water-saturated and in the oil-saturated media. However, we observe one tendency in the relative behavior of the P-wave attenuation between oil and full water saturations: At frequencies lower than the transition frequency of  $Q_P$  for the oil-saturated media, the P-wave attenuation tends to be higher in the oil-saturated media than in the fully water-saturated media, although the maximum values of P-wave attenuation can be higher or lower in the fully water-saturated media. More precisely, for cases A–D, the P-wave attenuation in the oil-saturated media is at least twice as high as in the water-saturated media at frequencies equal to or lower than the transition frequencies of  $Q_P$  in the oil-saturated media.

## MEDIA WITH ELLIPTICAL HETEROGENEITIES

### Experimental setup

We now investigate the effect of anisotropy on S-wave attenuation by replacing the mesoscopic-scale circular heterogeneities in the previous periodic model (with no permeability barriers) with elliptical ones. We calculate S-wave attenuation as a function of

the incidence angle for media containing periodically distributed elliptical heterogeneities whose unit cells are shown in Figure 6. The shear modulus at  $0^\circ$  incidence can be obtained with the simple shear experiment (Figure 2b) and equation 4. For calculating the shear modulus at different incidence angles, we assume that the medium with elliptical heterogeneities is a vertically transversely isotropic (VTI) medium (e.g., Wenzlau et al, 2010). The viscoelastic behavior of a 2D VTI medium is described by four independent components of the stiffness matrix,  $C_{11}$ ,  $C_{33}$ ,  $C_{44}$ , and  $C_{13}$ , which are used to calculate the shear modulus as a function of the incidence angle (Appendix A). To calculate the four components of the stiffness matrix, we perform the two relaxation experiments shown in Figure 2, which yield  $C_{33}$  and  $C_{44}$  (equations 3 and 4), and two additional experiments shown in Figure 7.

In the uniaxial compression test shown in Figure 7a, the function  $S(t)$  is attributed to the displacement in the  $x$ -direction at the right boundary of the numerical model and zero is attributed to the displacement in the  $x$ -direction at the left boundary and to the displacement in the  $z$ -direction at the top and bottom boundaries. Time-dependent normal stress and strain in the  $x$ -direction are obtained from this experiment. A partial time derivative is applied to these results; subsequently, the normal stress and strain rates in the  $x$ -direction are converted into the frequency domain, yielding  $\hat{\sigma}_{xx}$  and  $\hat{\epsilon}_{xx}$ . We then calculate the complex and frequency-dependent component:

$$C_{11} = \frac{\hat{\sigma}_{xx}}{\hat{\epsilon}_{xx}}. \quad (5)$$

In the mixed test shown in Figure 7b, a biaxial compression is simulated by attributing  $S(t)$  to the displacement in the  $z$ -direction at the top boundary,  $S(t)/2$  to the displacement in the  $x$ -direction at the right boundary, and zero to the displacement in the  $z$ -direction at the bottom boundary and to the displacement in the  $x$ -direction at the left boundary. Time-dependent normal stress and strain in

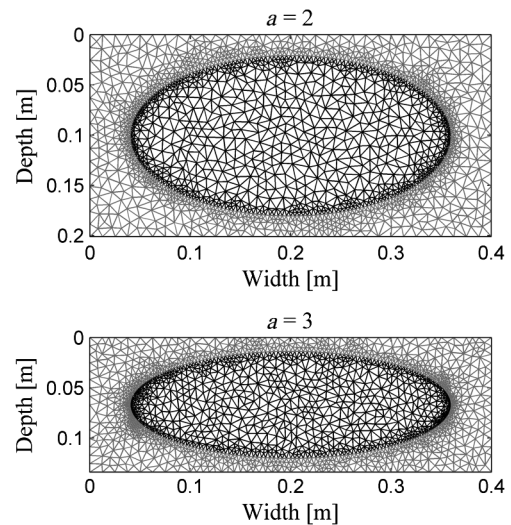


Figure 6. Unstructured finite-element meshes of the unit cell containing an elliptical heterogeneity with aspect ratio  $a = 2$  (top) and  $a = 3$  (bottom). Black and gray elements inside and outside the heterogeneity have different petrophysical properties (Tables 2 and 3). The spatial resolution of the meshes is higher close to the interfaces between the heterogeneities and the backgrounds.

$x$ - and  $z$ -directions are obtained from this experiment. A partial time derivative is applied to these results; subsequently, the normal stress and strain rates in the  $x$ - and  $z$ -directions are converted to the frequency domain, yielding  $\hat{\sigma}_{xx}$ ,  $\hat{\sigma}_{zz}$ ,  $\hat{\epsilon}_{xx}$ , and  $\hat{\epsilon}_{zz}$ . Using  $C_{33}$  and  $C_{11}$  obtained in the previous experiments, we obtain the complex and frequency-dependent component:

$$C_{13} = \frac{C_{11}\hat{\epsilon}_{xx} - C_{33}\hat{\epsilon}_{zz}}{\hat{\epsilon}_{xx} - \hat{\epsilon}_{zz}} \quad (6)$$

(e.g., Picotti et al., 2010).

The complex and frequency-dependent modulus  $\mu$  as function of incidence angle is calculated using the four components of the stiffness matrix  $C_{11}$ ,  $C_{33}$ ,  $C_{44}$ , and  $C_{13}$  as described in Appendix A (equations A-3 and A-4). The S-wave quality factor as function of incidence angle is calculated from  $\mu$ , using equation 2.

As for the media with circular heterogeneities, the elliptical heterogeneities are characterized by low permeability and low porosity, embedded in a background medium of high permeability and high porosity. The properties of the solid frame are those of case A (Table 3). The unit cell is a rectangle with the greater side equal to 40 cm, and the major semiaxis of the elliptical heterogeneity is 16 cm (Figure 6). By varying the minor semiaxis of the ellipse, two aspect ratios  $a$  (major semiaxis divided by minor semiaxis), are considered:  $a = 2$  and 3 (Figure 6). For both cases, the elliptical heterogeneity occupies 50% of the unit cell, which is achieved by accordingly setting the length of the shorter side of the rectangle. The pore space in the background corresponds to 80% of the total pore space in the medium. We perform simulations for media having heterogeneities always fully saturated with water and the background fully saturated with oil, gas, or water (Table 2), corresponding to three saturation scenarios: oil-saturated medium (80% oil, 20% water), gas-saturated medium (80% gas, 20% water), and fully water-saturated medium.

## Simulations and results

Simulations are performed for a medium consisting of periodically distributed elliptical heterogeneities of two aspect ratios (Figure 6), embedded in a homogeneous background. For each aspect ratio and each saturation scenario, four relaxation tests (Figures 2 and 7) are performed. The compression tests (Figures 2a, 7a, and 7b) are performed with a numerical model consisting of a single unit cell. The normal strains and stresses calculated from the compression tests are averaged over the area of the unit cell. The

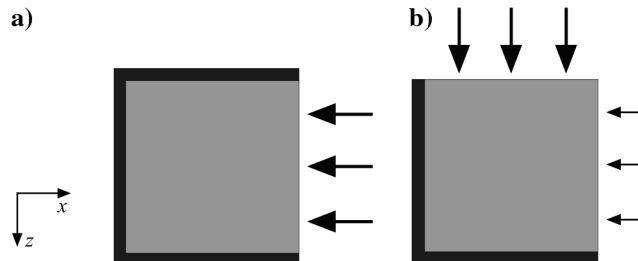


Figure 7. Sketch of the relaxation experiments: (a) uniaxial compression in the  $x$ -direction and (b) mixed compression test. The arrows indicate direction and magnitude of the displacements applied at the boundaries.

simple shear tests (Figure 2b) are performed with a numerical model consisting of a  $7 \times 7$  array of unit cells for  $a = 2$  and with a numerical model consisting of a  $9 \times 9$  array of unit cells for  $a = 3$ . The shear strains and stresses calculated from the simple shear tests are averaged over the area of only a single unit cell located in the center of the model. This is done to avoid the effects of the undrained boundary condition on the S-wave attenuation, as discussed in the previous section.

In Figure 8, we show the real part of the shear modulus  $\mu$  and the S-wave quality factor  $Q_S$  as functions of frequency at  $0^\circ$  (left) and  $45^\circ$  (right) incidence. The incidence angle is the angle between the wave vector and the (vertical)  $z$ -axis of symmetry. We observe approximately the same relative behavior of the S-wave attenuation among the three different saturation scenarios for  $a = 2$  and 3 and for  $0^\circ$  and  $45^\circ$  incidence. The plots for  $Q_S$  look similar with respect to the relative position of the three curves (three saturation scenarios), and similar to the plots for  $Q_S$  in Figure 5 (for circular heterogeneities). The S-wave attenuation in the gas-saturated media is very low and much lower than in the oil-saturated or in the fully water-saturated media. At low frequencies, the S-wave attenuation is significantly higher in the oil-saturated media than in the fully water-saturated media, although the maximum value of S-wave attenuation is higher in the fully water-saturated media. At frequencies equal to or lower than the transition frequencies of  $Q_S$  in the oil-saturated media, the S-wave attenuation is about one order of magnitude higher in the oil-saturated media than in the water-saturated media, and the transition frequencies of  $Q_S$  in the oil-saturated media are about 12 times lower than the transition frequencies of  $Q_S$  in the water-saturated media.

In Figure 9, we show the minimum values of  $Q_S$  and the frequencies at which they occur, referred to as transition frequencies  $f_{tr}$ , as functions of incidence angle for the three saturation scenarios. We can observe that the discussed relative behavior of the S-wave

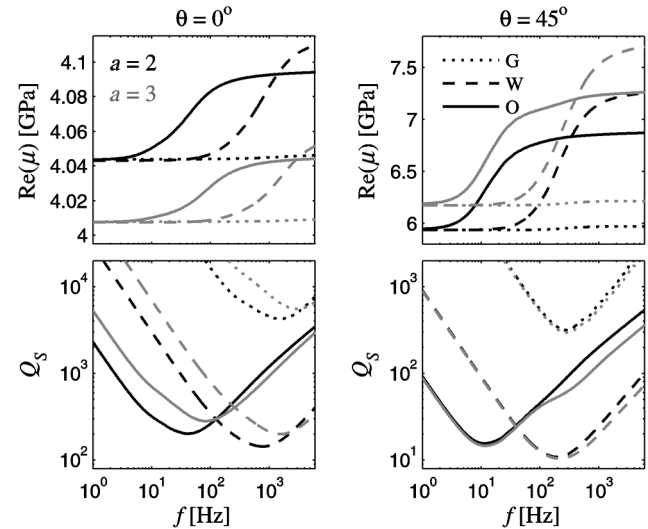


Figure 8. Numerical results for the real part of the shear modulus  $\mu$  and the S-wave quality factor  $Q_S$  as functions of frequency, at  $0^\circ$  (left) and  $45^\circ$  (right) incidence. The media contains periodically distributed elliptical heterogeneities with aspect ratios  $a = 2$  and 3 (indicated in black and gray, respectively). The three saturation scenarios (Table 2) are considered: gas-, water-, or oil-saturated background (dotted, dashed, or solid lines, respectively). The solid frame properties are described by case A in Table 3.

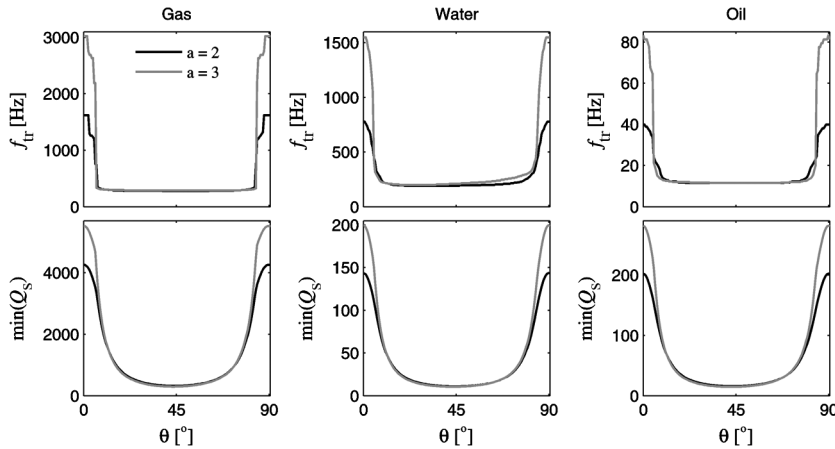


Figure 9. Numerical results for the minimum values of the frequency-dependent  $Q_S$ ,  $\min(Q_S)$ , and the frequencies at which these minima occur, referred to as transition frequencies  $f_{tr}$  as functions of incidence angle. The periodically distributed elliptical heterogeneities have aspect ratios  $a = 2$  and  $3$ , and each column refers to one of the three saturation scenarios (Table 2): gas-, water-, or oil-saturated background. The solid frame properties are described by case A in Table 3.

attenuation among the three different saturation scenarios takes place at all incidence angles.

At  $0^\circ$  incidence, the S-wave attenuation decreases with increasing aspect ratio (Figures 8 and 9). This is also the case when the aspect ratio  $a = 1$  (circular heterogeneity, Figure 5b). At  $45^\circ$  incidence, the S-wave attenuation in Figure 9 is highest and the minimum values of  $Q_S$  and their transition frequencies have the lowest dependency on the aspect ratio, with the minimum values of  $Q_S$  decreasing slightly with increasing aspect ratio. The minimum values of  $Q_S$  and the transition frequencies at  $45^\circ$  incidence for  $a = 2$  and  $3$ , respectively, are 316 at 275 Hz and 294 at 288 Hz for the gas-saturated medium, 10.8 at 191 Hz and 10.4 at 209 Hz for the fully water-saturated medium, and 15.5 at 11.5 Hz and 14.5 at 11.5 Hz for the oil-saturated medium. Notably, the S-wave attenuation can be very high in the oil-saturated medium and in the fully water-saturated medium at  $45^\circ$  incidence.

## DISCUSSION

The S-wave attenuation in this study is caused by flow of the pore fluid between the heterogeneity and the background. For the oil-saturated rock, fluid flow between the water-saturated heterogeneity and the oil-saturated background due to simple shear is shown in Figure 4b and 4c. In these simple shear experiments, the displacements in the  $x$ -direction applied at the top and bottom boundaries of the REV with different signs (Figure 2b) induce pore-fluid pressure differences (snapshots for  $P$  in Figure 4b and 4c). The resulting fluid pressure gradient causes flow of the pore fluid (snapshots for  $V_z$  and  $V_x$  in Figure 4b and 4c), which is responsible for energy loss (i.e., attenuation). The resulting S-wave attenuation is shown in Figure 5b and 5c.

At the quasi-static limit in Figures 5b, 5c, and 8, our results for the shear modulus  $\mu$  are independent of the properties of the saturating fluid. This is predicted by Gassmann's theory for the quasi-static mechanical behavior of fluid-saturated isotropic rocks (Gassmann, 1951; Berryman, 1999). For higher frequencies, our results for the value of  $\mu$  depend on fluid saturation, which is predicted by Berryman and Wang (2001) by applying an effective medium theory to poroelastic media consisting of a heterogeneous solid frame. Even though the effective medium theory is a low-frequency method, it is pertinent to a higher frequency band than the quasi-static limit. At these higher frequencies, Berryman and Wang (2001) discuss that the external shear boundary conditions can lead to local compression in some regions containing liquid. Because the

liquid can support compression (but not shear), it stores some of the energy resulting from the shear boundary conditions; therefore the shear modulus depends on fluid properties. In this study, we explain such frequency-dependent fluid effect on the value of  $\mu$  (i.e., dispersion) by attenuation of S-waves due to wave-induced fluid flow.

The observed consistent tendency in the relative behavior of the S-wave attenuation among the different saturation scenarios (Figures 5, 8, and 9) is related to this unilateral frequency dependence of  $\mu$  on fluid properties. Because its value at the low-frequency limit is the same for all fluids, the fluid effect on S-wave attenuation is only controlled by the high-frequency limit of  $\mu$  but not by the low-frequency limit as long as the media only differ in fluid saturation. The relative behavior of the P-wave attenuation among the different saturation scenarios is more variable and more complicated because both low- and high-frequency limits of the P-wave modulus  $H$  depend on fluid properties.

It is known that a medium with a homogeneous frame, partially (patchy) saturated with water and gas, may exhibit high P-wave attenuation when it has a low gas saturation of around 10% (e.g., Quintal et al., 2009) but very low P-wave attenuation for large amounts of gas. However, when the medium has a heterogeneous frame (double porosity) in addition to patchy saturation, as in our models, more parameters control the compressibility and fluid mobility ( $k/\eta$ ) in the different regions, and the P-wave attenuation can be high for large (80%) gas or even oil saturations, as we observe in Figure 5a for case D. In case D, the P-wave quality factor in the gas- and in the oil-saturated media is  $Q_P = 5.7$  and 12, respectively, at about 15 Hz.

## CONCLUSIONS

Relaxation experiments have been numerically performed to calculate P- and S-wave attenuation due to wave-induced fluid flow in poroelastic media containing periodically distributed heterogeneities in a permeable homogeneous background. We have studied the influence of undrained boundary conditions for numerical models consisting of a single unit cell or several unit cells of such a periodic medium. No effect is expected for P-wave attenuation, and a single undrained unit cell can be used to represent a medium with periodically distributed heterogeneities. However, the undrained boundary condition causes a significant increase in S-wave attenuation when the numerical model consists of only a single unit cell. Shear relaxation experiments simulated to calculate S-wave attenuation in a periodic medium with permeable homogeneous background require numerical models composed of several unit

cells or another type of boundary condition. This also shows that a fluid-saturated medium will have significantly increased S-wave attenuation in regions surrounded by impermeable barriers. This suggests that S-wave attenuation could be an indicator of permeability changes in, for example, fracturing operations.

We have explained the dependence of the shear modulus on the fluid saturation at frequencies higher than the quasi-static limit by S-wave attenuation due to wave-induced fluid flow at the mesoscopic scale. The S-wave attenuation due to this mechanism in a medium with heterogeneous solid frame exhibits a consistent tendency in its relative behavior among different saturation scenarios (80% oil, 20% water; 80% gas, 20% water; and 100% water). First, the S-wave attenuation in the gas-saturated media is very low and much lower than in the oil-saturated or in the fully water-saturated media. Second, at low frequencies, the S-wave attenuation is significantly higher in the oil-saturated media than in the fully water-saturated media. This tendency is observed for media containing periodically distributed heterogeneities, considering four sets of rock-frame parameters and both circular and elliptical heterogeneities for different incidence angles.

The P-wave attenuation, which is more commonly used as a fluid indicator, exhibits a more variable relative behavior among the different saturation scenarios, strongly depending on the rock-frame properties. However, for four sets of rock-frame parameters and circular heterogeneities, we observe one tendency in the relative behavior of the P-wave attenuation between oil- and full water saturations: At low frequencies, the P-wave attenuation tends to be higher in the oil-saturated media than in the fully water-saturated media.

Based on these relative behaviors of P- and S-wave attenuation, we suggest that S-wave attenuation could be used as an indicator of fluid content in a reservoir in addition to P-wave attenuation. For example, spectral decomposition could be applied to seismic P- and S-wave data to help distinguish between oil and water content because at low frequencies attenuation of P- and S-waves tends to be higher in oil-saturated (80% oil, 20% water) media than in media fully saturated with water, according to the physical mechanism of wave-induced fluid flow.

## ACKNOWLEDGMENTS

This work has been supported by the Low Frequency Seismic Partnership (LFSP) and Spectraseis. E. H. Saenger thanks the German Research Foundation (DFG) for support through the Heisenberg scholarship SA 996/1-2. B. Quintal thanks Marc-André Lambert for very decisive suggestions and discussions.

## APPENDIX A

### VOIGT STIFFNESS MATRIX FOR VTI MEDIA

Hooke's law for a VTI, linear solid in Voigt notation is

$$\begin{bmatrix} \sigma_{xx} \\ \sigma_{yy} \\ \sigma_{zz} \\ \sigma_{yz} \\ \sigma_{xz} \\ \sigma_{xy} \end{bmatrix} = \begin{bmatrix} C_{11} & C_{12} & C_{13} & 0 & 0 & 0 \\ C_{12} & C_{11} & C_{13} & 0 & 0 & 0 \\ C_{13} & C_{13} & C_{33} & 0 & 0 & 0 \\ 0 & 0 & 0 & C_{44} & 0 & 0 \\ 0 & 0 & 0 & 0 & C_{44} & 0 \\ 0 & 0 & 0 & 0 & 0 & C_{66} \end{bmatrix} \begin{bmatrix} \varepsilon_{xx} \\ \varepsilon_{yy} \\ \varepsilon_{zz} \\ 2\varepsilon_{yz} \\ 2\varepsilon_{xz} \\ 2\varepsilon_{xy} \end{bmatrix}, \quad (\text{A-1})$$

taking into account the symmetry of stresses and strains (Mavko et al., 2009). Knowing that

$$C_{66} = \frac{C_{11} - C_{22}}{2}, \quad (\text{A-2})$$

the number of independent components of the stiffness matrix is five. If the solid is viscoelastic, the components of the stiffness matrix are complex. The heterogeneous poroelastic media in our simulations behave viscoelastically. Because we consider 2D VTI models in the  $x$ - $z$ -plane, we only need to determine the four components  $C_{11}$ ,  $C_{33}$ ,  $C_{44}$ , and  $C_{13}$ .

To calculate the shear modulus in the  $x$ - $z$ -plane for a VTI medium, we use

$$\mu = \frac{1}{2} (C_{11} \sin^2 \theta + C_{33} \cos^2 \theta + C_{44} - \sqrt{M}), \quad (\text{A-3})$$

where

$$M = ((C_{11} - C_{44})\sin^2 \theta - (C_{33} - C_{44})\cos^2 \theta)^2 + (C_{13} + C_{44})^2 \sin^2 2\theta \quad (\text{A-4})$$

and  $\theta$  is the incidence angle, that is, the angle between the wave vector and the  $z$ -axis of symmetry (Mavko et al., 2009).

## REFERENCES

- Batzle, M., and Z. Wang, 1992, Seismic properties of pore fluids: *Geophysics*, **57**, 1396–1408, doi: [10.1190/1.1443207](https://doi.org/10.1190/1.1443207).
- Behura, J., M. Batzle, R. Hofmann, and J. Dorgan, 2009, The shear properties of oil shales: The Leading Edge, **28**, 850–855, doi: [10.1190/1.3167788](https://doi.org/10.1190/1.3167788).
- Berryman, J. G., 1999, Origin of Gassmann's equations: *Geophysics*, **64**, 1627–1629, doi: [10.1190/1.1444667](https://doi.org/10.1190/1.1444667).
- Berryman, J. G., and H. F. Wang, 2001, Dispersion in poroelastic systems: *Physical Review E*, **64**, no. 1, 011303, doi: [10.1103/PhysRevE.64.011303](https://doi.org/10.1103/PhysRevE.64.011303).
- Biot, M. A., 1941, General theory of three-dimensional consolidation: *Journal of Applied Physics*, **12**, 155–164, doi: [10.1063/1.1712886](https://doi.org/10.1063/1.1712886).
- Biot, M. A., 1962, Mechanics of deformation and acoustic propagation in porous media: *Journal of Applied Physics*, **33**, 1482–1498, doi: [10.1063/1.1728759](https://doi.org/10.1063/1.1728759).
- Bourbié, T., O. Coussy, and B. Zinszner, 1987, *Acoustics of porous media*: Editions Technip.
- Carcione, J. M., 2007, *Wave fields in real media: Theory and numerical simulation of wave propagation in anisotropic, anelastic, porous and electromagnetic media*: Elsevier.
- Chapman, M., E. Liu, and X. Li, 2006, The influence of fluid-sensitive dispersion and attenuation on AVO analysis: *Geophysical Journal International*, **167**, 89–105, doi: [10.1111/gji.2006.167.issue-1](https://doi.org/10.1111/gji.2006.167.issue-1).
- Gassmann, F., 1951, Über die elastizität poröser medien: *Vierteljahrschrift der Naturforschenden Gesellschaft in Zürich*, **96**, 1–23.
- Johnson, D. L., 2001, Theory of frequency dependent acoustics in patchy-saturated porous media: *Journal of the Acoustical Society of America*, **110**, 682–694, doi: [10.1121/1.1381021](https://doi.org/10.1121/1.1381021).
- Liu, X., S. Greenhalgh, and B. Zhou, 2009, Scattering of plane transverse waves by spherical inclusions in a poroelastic medium: *Geophysical Journal International*, **176**, 938–950, doi: [10.1111/gji.2009.176.issue-3](https://doi.org/10.1111/gji.2009.176.issue-3).
- Masson, Y. J., and S. R. Pride, 2007, Poroelastic finite-difference modeling of seismic attenuation and dispersion due to mesoscopic-scale heterogeneity: *Journal of Geophysical Research*, **112**, B03204, doi: [10.1029/2006JB004592](https://doi.org/10.1029/2006JB004592).
- Mavko, G., T. Mukerji, and J. Dvorkin, 2009, *The rock physics handbook: Tools for seismic analysis of porous media*, 2nd ed.: Cambridge University Press.
- Müller, T. M., and B. Gurevich, 2004, One-dimensional random patchy saturation model for velocity and attenuation in porous rocks: *Geophysics*, **69**, 1166–1172, doi: [10.1190/1.1801934](https://doi.org/10.1190/1.1801934).
- Müller, T. M., B. Gurevich, and M. Lebedev, 2010, Seismic wave attenuation and dispersion resulting from wave-induced flow in porous rocks — A review: *Geophysics*, **75**, no. 5, A147–A164, doi: [10.1190/1.3463417](https://doi.org/10.1190/1.3463417).

- Norris, A. N., 1993, Low-frequency dispersion and attenuation in partially saturated rocks: *Journal of the Acoustical Society of America*, **94**, no. 1, 359–370, doi: [10.1121/1.407101](https://doi.org/10.1121/1.407101).
- Paffenholz, J., and H. Burkhardt, 1989, Absorption and modulus measurements in the seismic frequency and strain range on partially saturated sedimentary rocks: *Journal of Geophysical Research*, **94**, 9493–9507, doi: [10.1029/JB094iB07p09493](https://doi.org/10.1029/JB094iB07p09493).
- Picotti, S., J. M. Carcione, J. E. Santos, and D. Gei, 2010,  $Q$ -anisotropy in finely-layered media: *Geophysical Research Letters*, **37**, L06302, doi: [10.1029/2009GL042046](https://doi.org/10.1029/2009GL042046).
- Pride, S. R., and J. G. Berryman, 2003a, Linear dynamics of double-porosity and dual-permeability materials. I. Governing equations and acoustic attenuation: *Physical Review E*, **68**, 036603, doi: [10.1103/PhysRevE.68.036603](https://doi.org/10.1103/PhysRevE.68.036603).
- Pride, S. R., and J. G. Berryman, 2003b, Linear dynamics of double-porosity and dual-permeability materials. II. Fluid transport equations: *Physical Review E*, **68**, 036604, doi: [10.1103/PhysRevE.68.036604](https://doi.org/10.1103/PhysRevE.68.036604).
- Pride, S. R., J. G. Berryman, and J. M. Harris, 2004, Seismic attenuation due to wave-induced flow: *Journal of Geophysical Research*, **109**, B01201, doi: [10.1029/2003JB002639](https://doi.org/10.1029/2003JB002639).
- Quintal, B., S. M. Schmalholz, and Y. Y. Podladchikov, 2009, Low-frequency reflections from a thin layer with high attenuation caused by interlayer flow: *Geophysics*, **74**, no. 1, N15–N23, doi: [10.1190/1.3026620](https://doi.org/10.1190/1.3026620).
- Quintal, B., S. M. Schmalholz, and Y. Y. Podladchikov, 2011a, Impact of fluid saturation on the reflection coefficient of a poroelastic layer: *Geophysics*, **76**, no. 2, N1–N12, doi: [10.1190/1.3553002](https://doi.org/10.1190/1.3553002).
- Quintal, B., H. Steeb, M. Frehner, and S. M. Schmalholz, 2011b, Quasi-static finite-element modeling of seismic attenuation and dispersion due to wave-induced fluid flow in poroelastic media: *Journal of Geophysical Research*, **116**, B01201, doi: [10.1029/2010JB007475](https://doi.org/10.1029/2010JB007475).
- Rapoport, M. B., L. I. Rapoport, and V. I. Ryjkov, 2004, Direct detection of oil and gas fields based on seismic inelasticity effect: *The Leading Edge*, **23**, 276–278, doi: [10.1190/1.1690901](https://doi.org/10.1190/1.1690901).
- Rubino, J. G., C. L. Ravazzoli, and J. E. Santos, 2009, Equivalent viscoelastic solids for heterogeneous fluid-saturated porous rocks: *Geophysics*, **74**, no. 1, N1–N13, doi: [10.1190/1.3008544](https://doi.org/10.1190/1.3008544).
- Rubino, J. G., D. R. Velis, and M. D. Sacchi, 2011, Numerical analysis of wave-induced fluid flow effects on seismic data: Application to monitoring of CO<sub>2</sub> storage at the Sleipner field: *Journal of Geophysical Research*, **116**, B03306, doi: [10.1029/2010JB007997](https://doi.org/10.1029/2010JB007997).
- Shewchuk, J. R., 2002, Delaunay refinement algorithms for triangular mesh generation: *Computational Geometry: Theory and Applications*, **22**, no. 1–3, 21–74, doi: [10.1016/S0925-7721\(01\)00047-5](https://doi.org/10.1016/S0925-7721(01)00047-5).
- Vogelaar, B., D. Smeulders, and J. Harris, 2010, Exact expression for the effective acoustics of patchy-saturated rocks: *Geophysics*, **75**, no. 4, N87–N96, doi: [10.1190/1.3463430](https://doi.org/10.1190/1.3463430).
- Wenzlau, F., J. B. Altmann, and T. M. Müller, 2010, Anisotropic dispersion and attenuation due to wave-induced fluid flow: Quasi-static finite element modeling in poroelastic solids: *Journal of Geophysical Research*, **115**, B07204, doi: [10.1029/2009JB006644](https://doi.org/10.1029/2009JB006644).
- White, J. E., 1975, Computed seismic speeds and attenuation in rocks with partial gas saturation: *Geophysics*, **40**, 224–232, doi: [10.1190/1.1440520](https://doi.org/10.1190/1.1440520).
- White, J. E., N. G. Mikhaylova, and F. M. Lyakhovitskiy, 1975, Low-frequency seismic waves in fluid saturated layered rocks: *Physics of the Solid Earth*, **11**, 654–659.
- Zienkiewicz, O. C., and T. Shiomi, 1984, Dynamic behaviour of saturated porous media: The generalized Biot formulation and its numerical solution: *International Journal for Numerical and Analytical Methods in Geomechanics*, **8**, no. 1, 71–96, doi: [10.1002/\(ISSN\)1096-9853](https://doi.org/10.1002/(ISSN)1096-9853).